Results in Engineering 27 (2025) 106117

Contents lists available at ScienceDirect

Results in Engineering

journal homepage: www.sciencedirect.com/journal/results-in-engineering

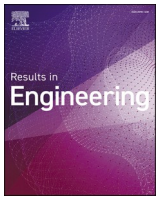

Research paper

# On the effectiveness of ABH-based metamaterials in vibration control of naval equipment subjected to underwater explosion loads

Jacopo Bardiani [a,*], Giada Kyaw Oo D'Amore [b], Giovanni Marchesi [a], Marco Biot [b], Claudio Sbarufatti [a], Andrea Manes [a]

[a] Department of Mechanical Engineering, Politecnico di Milano, Via G. La Masa 1, Milano 20156, Italy
[b] Department of Engineering and Architecture, University of Trieste, Via A. Valerio 6, Trieste 34127, Italy

ARTICLE INFO

*Keywords:*
Underwater explosion
Acoustic-structural simulation
Metamaterials
Acoustic black holes
Vibration control
Equipment safeguard

ABSTRACT

The dynamic response of marine structures to underwater explosions (UNDEX) is crucial for ensuring onboard equipment's operational safety and reliability. Non-contact UNDEX events generate shock waves and bubble oscillations that induce vibrations propagating through the hull, potentially affecting sensitive systems. This study proposes a novel numerical framework integrating a high-fidelity acoustic-structural coupled model (CASA) with an Acoustic Black Hole (ABH)-based metamaterial solution to enhance vibration mitigation. A validated finite element model of a full-scale patrol vessel is used to assess the frequency response of equipment mounted on traditional resilient supports. The innovation lies in the integration of ABH into the mounting system, forming a passive control solution tailored to reduce UNDEX-induced excitations. Comparative analyses between conventional mountings and the proposed configuration show that the ABH-based metamaterial effectively attenuates vibrations above its theoretical cut-on frequency, leading to reductions up to 20 m/s$^2$ in acceleration amplitude and an average peak attenuation of approximately 61 %. This work represents the first application of ABH technology in a naval context for mitigating UNDEX effects, offering a promising strategy for improving onboard equipment protection.

## 1. Introduction

Marine structures are exposed to a wide range of dynamic loads—including wave impact, slamming, and accidental events such as collisions or explosions—which can lead to various structural consequences such as deformation, fatigue damage, or even crack initiation and propagation [1–3].

Understanding the dynamic response of floating and submerged structures to pressure loads is essential for ensuring safety and structural integrity in the naval shipbuilding and offshore engineering industries. Among the various types of pressure loads that marine structures may experience, underwater explosions (UNDEX) are particularly critical due to their significant impact on safety and operational performance [4–8].

UNDEX are classified as either contact or non-contact, depending on whether the structure is within the bubble's immediate impact zone [9–12]. Contact explosions occur when explosives detonate near the hull, often causing severe structural damage, such as hull ruptures. In contrast, non-contact explosions, which occur farther from the target structure, may not compromise the hull's integrity but can still result in plastic and elastic deformations.

In a non-contact UNDEX, two main sources of loading actions can be identified: the primary shock waves and the subsequent gas bubble pulsation [10,13]. In addition to causing permanent deformation, the primary shock waves excite the hull of the vessel over a broad frequency range, with the induced vibrations propagating throughout the ship's structure. These vibrations can reach areas far from the impact point, inducing high-frequency responses in onboard equipment [14]. In contrast, gas bubble oscillations occur at lower frequencies and can result in dangerous global motions, such as whipping [13,15,16]. The present study addresses the non-contact UNDEX scenario, with particular emphasis on the frequency response of onboard equipment. This aspect is crucial, as the structural integrity and correct functioning of such equipment play a key role in ensuring the operability and safety of ships and offshore structures, especially when operating in harsh and dynamically demanding environments [17,18].

Currently, onboard equipment is protected from shock loads and

* Corresponding author.
*E-mail address:* jacopo.bardiani@polimi.it (J. Bardiani).

https://doi.org/10.1016/j.rineng.2025.106117
Received 25 May 2025; Received in revised form 3 July 2025; Accepted 3 July 2025
Available online 4 July 2025

vibrations using resilient mountings, which can be designed to deform either elastically or elastic-plastically (*i.e.*, requiring replacement after a shock event). These mountings are critical for isolating equipment from the dynamic disturbances encountered in naval environments, including those induced by UNDEX. The design and effectiveness of resilient mounting depend on several factors, such as their function (*i.e.,* anti-shock or anti-vibration), positioning, stiffness of the system, target frequency range, and the mass of the equipment. Moreover, the performance of these mountings is influenced by environmental conditions, operational loads, and aging. Thus, rigorous testing and qualification processes are needed. As a result, naval shipyards have a strong interest in researching advanced technologies that can provide more reliable, efficient, and durable solutions for equipment protection under dynamic loading conditions [19].

In response to these growing demands, recent research has increasingly focused on innovative materials and structural solutions aimed at improving vibration control performance. Among the various strategies investigated, particular interest has been directed toward advanced architected materials with unconventional dynamic properties (like metamaterials, etc.), capable of effectively absorbing and dissipating vibrational energy [20]. Although these solutions are still at an early stage of development and not yet widely adopted in industrial practice, promising applications have been documented in fields such as offshore structures [21], construction [22], and automotive engineering [23].

One of the most innovative vibration-reduction technologies found in the literature is the Acoustic Black Hole (ABH), which can be assembled in a metamaterial-inspired design. The ABH acts as a flexural wave trap, dissipating energy through damping materials placed in the ABH region [24].

Several prototyping applications of ABH for vibration and structure-borne noise reduction are presented in the literature [25–27]. However, despite their demonstrated potential in noise and vibration control, limited studies in marine engineering field are present in the available literature [28,29]. No studies have specifically addressed mitigating UNDEX effects on ship hulls.

This study explores the feasibility of employing ABH-based protective solutions to enhance the resilience of onboard equipment, with the goal of reducing vibrational energy transmission.

In this context, a novel numerical framework is proposed, integrating high-fidelity finite element modeling with ABH-based metamaterial for passive control of vibration. The originality of the approach lies in the combination of a validated global-scale numerical model of a real patrol vessel and the design of an ABH-based solution with a metamaterial-like pattern, improving the vibration damping performance of conventional resilient mounting systems.

The key innovations of this study are highlighted:

- Development of a coupled acoustic-structural approach (CASA) high-fidelity numerical model of a full-scale real patrol vessel subjected to far-field non-contact UNDEX loading. The model includes detailed structural features and has been validated by comparing its vibrational modes with experimental measurements (through Operational Modal Analysis, OMA), ensuring accurate dynamic response representation.
- Evaluation of the effectiveness of the currently adopted solution (*i.e.*, Vulkan resilient mountings) on vessels for equipment decoupling and protection by UNDEX loading. This is achieved through a high-fidelity modeling of a representative foundation–resilient–mass subsystem, analyzed in three different installation locations within the vessel and evaluating the frequency response of onboard equipment and their foundations.
- Design of an ABH-based passive control system aimed at attenuating vibrations induced by UNDEX loading, introduced to enhance the damping performances of the traditional mountings. A comparative analysis is carried out between the baseline configuration and the proposed one. To the best of the authors' knowledge, this represents the first application of an ABH concept within a naval context to mitigate the vibrational effects of UNDEX on onboard equipment.

The insights and methodologies developed in this study contribute to safer and more efficient vibration protection strategies for onboard equipment in naval and offshore structures. By enhancing the damping performance of traditional resilient systems through the integration of ABH-based metamaterials, the proposed approach supports the development of more robust and cost-effective solutions against UNDEX-induced excitations. Beyond its immediate application to naval vessels, this methodology has broader implications for vibration mitigation in critical engineering systems where reliability and structural integrity are paramount, including offshore platforms, underwater vehicles, and marine energy infrastructures.

To effectively evaluate the impact of ABH-based solutions under realistic UNDEX loading conditions, a robust and versatile numerical simulation framework is required, especially in the case of full-scale marine structure [30]. Among the available numerical approaches, the explicit finite element method has been widely adopted to capture the transient, nonlinear structural response to blast loading in various contexts, including civil infrastructures and naval applications [31–36]. Various studies in literature used commercial FEM software such as LS-DYNA, ABAQUS, ANSYS, and MSC Dytran to accurately predict transient loading and the structural responses of marine structures subjected to different UNDEX scenarios [37,38]. Among the various available approaches, coupled numerical methods are most employed to study transient Fluid-Structure Interaction (FSI) during UNDEX, thanks to their reliable results [15,39]. In this context, a widely used approach is the CASA method developed in ABAQUS CAE commercial suite. This approach has become increasingly popular in recent years due to its reduced computational cost compared to other coupled strategies [40–44]. Indeed, the simulation does not model the explosion and the pressure wave propagation in the far field but uses an acoustic field initialization [45]. This initialization is performed by setting a time trace of the pressure wave propagation, which can either be recorded in real time [46] or calculated using analytical methods [9,47]. Since the CASA approach has already demonstrated its accuracy against experimental conditions [40,48,49], and the structural model of the vessel has been validated with respect to its experimentally identified vibration modes, the reliability of the comparative analysis aimed at evaluating the effectiveness of the ABH-based solution in enhancing the vibration mitigation performance of the traditional mounting system is ensured.

The paper is structured as follows. The fundamental background theory for the simulations performed in ABAQUS CAE commercial suite is presented in Section 2. Section 3 describes the target ship used as a case study and the experimental tests conducted to evaluate its natural modes. The numerical model for UNDEX simulation is introduced in Section 4, while the use of the ABH for vibration control is explained in Section 5. Finally, the results are discussed in Section 6, and the conclusions of the present research are summarized in Section 7.

## 2. The coupled acoustic-structural approach in abaqus CAE

The coupled acoustic-structural method for the ABAQUS/Explicit solver is extensively covered in the literature and is detailed in the Abaqus Analysis User's Guide, as mentioned in the introductory section. Thus, only some of the most important theories and settings are outlined in the present work. For further details regarding the mathematical formulation of this approach, refer to [45].

The equilibrium equation for small movements of a compressible, adiabatic fluid with velocity-dependent momentum losses is expressed in Eq. (1):

$$\frac{\partial p}{\partial x} + \gamma(x,\theta_i)\dot{u}^f + \rho_f(x,\theta_i)\ddot{u}^f = 0 \tag{1}$$


**Fig. 1.** Picture of the Swedish patrol vessel KBV 202, from which the numerical model of the present research takes inspiration.

where $p$ is the excess pressure in the fluid (*i.e.,* the pressure in excess of any static pressure), $x$ is the spatial position of the fluid particle, $\dot{u}^f$ is the fluid particle velocity, $\ddot{u}^f$ is the fluid particle acceleration, $\rho_f$ is the density of the fluid, $\gamma$ is the "volumetric drag" (*i.e.*, force per unit volume per velocity), and $\theta_i$ are $i$-independent field variables such as temperature, humidity of air, or salinity of water on which $\rho_f$ and $\gamma$ may depend. The d'Alembert term is written without convection consistently with the assumption that there is no steady flow of the fluid. This is usually considered sufficiently accurate for steady fluid velocities up to Mach 0.1.

The constitute response of the fluid is assumed to be inviscid, linear, and compressible, so the excess pressure in the fluid can be written as Eq. (2):

$$p = -K_f(x, \theta_i)\frac{\partial}{\partial x}u^f \tag{2}$$

where $K_f$ is the bulk modulus of the fluid and $u^f$ is the fluid particle displacement, while the quantity $x$ and $\theta_i$ have been already defined.

The constitutive behavior for an acoustic medium that can undergo cavitation can be described as follows: the absolute pressure (*i.e.*, the sum of static and excess dynamic pressures) is restricted from falling below a defined cavitation threshold. When the absolute pressure reaches this threshold, the medium is considered to enter a state of free expansion, wherein dynamic pressure does not further decrease. As this free expansion is reversed and volumetric strain reduces to the level associated with the cavitation threshold, the pressure within the medium starts to rebuild. This is expressed through the following relation:

$$p = max\{p_v, p_c - p_0\} \tag{3}$$

where a pseudo-pressure $p_v$, a measure of the volumetric strain, is calculated through Eq. (2), $p_c$ is the fluid cavitation limit and $p_0$ is the initial acoustic static pressure. A total wave formulation is employed for a nonlinear acoustic medium experiencing cavitation. It is important to note that this total wave approach closely resembles the scattered wave formulation, except that the pseudo-pressure (defined as the product of the bulk modulus and the compressive volumetric strain) serves as the material state variable in place of the acoustic excess pressure. The acoustic excess pressure can be directly derived from this pseudo-pressure under the cavitation condition.

For what concerns the control equation of the structure embedded in the fluid domain, Eq. (4) is employed [50,51]:

$$[M_s]\{\ddot{u}\} + [C_s]\{\dot{u}\} + [K_s]\{u\} = \{f_{out}\} \tag{4}$$

where $[M_s]$ is the mass matrix, $[C_s]$ is the damping matrix, $[K_s]$ is the stiffness matrix, $\{u\}$ is the displacement vector, $\{\dot{u}\}$ is the velocity vector, $\{\ddot{u}\}$ is the acceleration vector and finally $\{f_{out}\}$ is the external force vector acting on the structure. $\{f_{out}\}$ can be written as follows:

$$\{f_{out}\} = -[G]\left[A_f\right](\{P_r\} + \{P_s\} + \{P_{st}\}) \tag{5}$$

where $\{P_r\}$ is the incident wave pressure, $\{P_s\}$ is the scattered wave pressure, $\{P_{st}\}$ is the initial pressure (*i.e.*, hydrostatic one), $[G]$ is the transformation matrix related to surface forces of structure and fluid nodes and finally $\left[A_f\right]$ is the diagonal area matrix related to an element in the fluid mesh.

At the interface, acoustic and structural surfaces are coupled, and the coupling force is calculated using the penalty method [45].

In this approach, a significant choice that should be made is related to the type of acoustic wave formulation used in the analysis. Both scattered [41,42] and total [43,44] wave formulations have been extensively applied in UNDEX studies.

In the total wave formulation, a time-varying load is applied at the outer boundary of the acoustic medium, generating a response within it and inducing shock loading on the structure. This load is typically based on a calculated pressure-time history using empirical formulas or field/laboratory UNDEX tests [9,47]. In contrast, the scattered wave formulation applies loading to both the acoustic and structural interface surfaces. The acoustic pressure degree of freedom in this case represents only the scattered portion of the total pressure, excluding the incident wave contribution. Therefore, a free-field pressure history, as predicted by empirical formulas or tests, is not entirely applicable for scattered loading input, since the reflected wave at the acoustic-structural interface does not perfectly replicate the incident wave. Additionally, in the scattered wave algorithm, the standoff point for defining the UNDEX loading history is typically placed on or near the structural surface, whereas in the total wave algorithm, it is placed on the outer acoustic surface closest to the source. The total wave algorithm is necessary when the acoustic medium becomes nonlinear due to fluid cavitation, which occurs when the pressure in the flow field drops below the saturation vapor pressure (approximately 30.4 kPa). Choosing the appropriate wave algorithm is critical for numerical accuracy, and the results from both formulations should be compared to determine the most suitable approach for a given scenario [45].

## 3. The target ship and the experimental tests

A demonstrative geometry of the Swedish patrol vessel KBV 202 (Fig. 1), part of the KBV 201 class, is employed for calculations in the presented work. Built at the Kockums shipyard and delivered in 2002, KBV 202 is primarily used for patrolling and environmental cleanup operations, including oil spill sanitation. The vessel has a displacement of 4670 kN and measures 52 m in length with a breadth of 8.6 m. The design draft is approximately 3.2 m, and the maximum speed is around 21 knots.

The vessel presents a mixed reinforcement structure, incorporating longitudinal and transverse girders. Details such as the thickness of the structural elements are not reported in the paper due to confidentiality restrictions.

Saab and SVIBS companies performed an OMA on this vessel in late October and the first week of November 2023. The tests took place in the Gulf of Bothnia, on the east coast of Sweden.

The measurement setup is dictated by the need to perform measurements during the vessel's normal operations. Fig. 2(a) reports the sensors positioning. The sensors 3–5 and 8–10 were mounted on the main deck, close to the toerail, while sensors 1,2,6 and 7 were mounted on the lower deck. A Dewesoft IOLITE mems triaxial accelerometer (Fig. 2(b)) was mounted at each location with four magnets. The DewesoftX data acquisition system was used to register the data.

The OMA was made using ARTeMIS Modal Pro suite. Three different methods were applied to calculate the vibrational modes of the vessel [52,53]: the Enhanced Frequency Domain Decomposition (EFDD), the Curve-fit Frequency Domain Decomposition (CFDD) and finally the Stochastic Subspace Identification - Extended Unweighted Principal

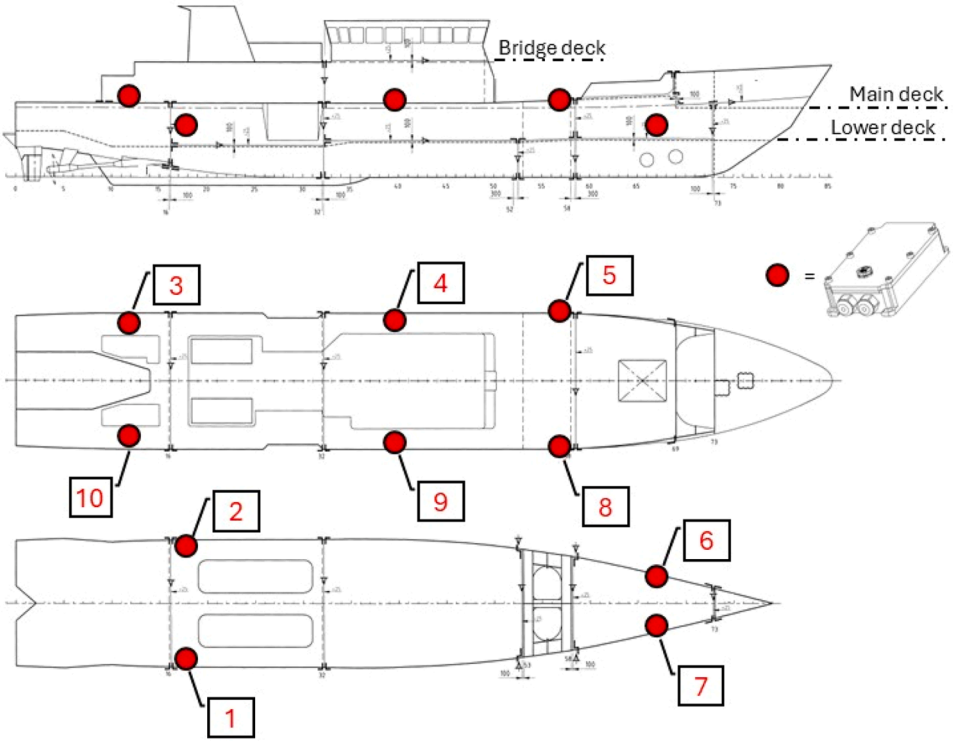


(a)

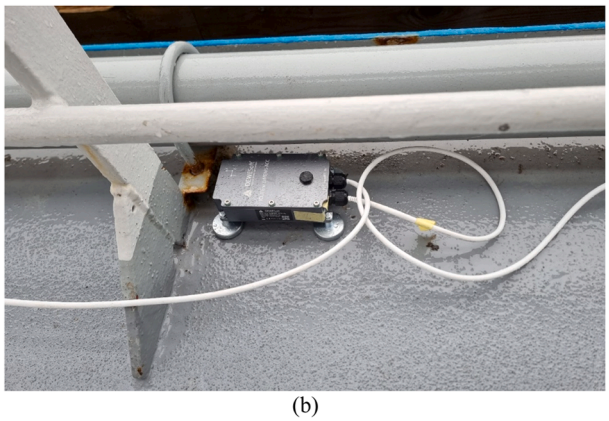

(b)

**Fig. 2.** (a) Sensor positions and (b) Dewesoft IOLITE mems triaxial accelerometer.

**Table 1**
1° hull mode (vertical bending) obtained through EFDD, CFDD and SSI-UPCX methods.

| Method | Frequency [Hz] | Damping ratio [ %] | Complexity [ %] |
|---|---|---|---|
| EFDD | 4.028 | 1.8 | 0.1 |
| CFDD | 4.025 | 1.4 | 0.1 |
| SSI-UPCX | 4.025 | 2.1 | 0.9 |

**Table 2**
2° hull mode (horizontal bending) obtained through EFDD, CFDD and SSI-UPCX methods.

| Method | Frequency [Hz] | Damping ratio [ %] | Complexity [ %] |
|---|---|---|---|
| EFDD | 7.400 | 0.04 | 32 |
| CFDD | 7.398 | 0.08 | 32 |
| SSI-UPCX | 7.398 | 0.10 | 31 |

**Table 3**
3° hull mode (torsional) obtained through EFDD, CFDD and SSI-UPCX methods.

| Method | Frequency [Hz] | Damping ratio [ %] | Complexity [ %] |
|---|---|---|---|
| EFDD | 7.869 | 1.33 | 4.9 |
| CFDD | 7.882 | 1.08 | 4.9 |
| SSI-UPCX | 7.947 | 2.10 | 9.0 |

Component (SSI-UPCX).

The combined use of EFDD, CFDD, and SSI-UPCX allows for a more robust and accurate characterization of the ship's vibration modes by leveraging the strengths of each method. EFDD and CFDD operate in the frequency domain, identifying natural frequencies and mode shapes from the power spectral density, while SSI-UPCX works in the time domain, making it particularly effective in distinguishing closely spaced modes and reducing the influence of noise. The choice to apply multiple techniques ensures consistency and helps mitigate uncertainties arising from the ship's real operational conditions, ultimately improving the reliability of the modal analysis.

The first three experimental hull modes are listed in Table 1–3. Each

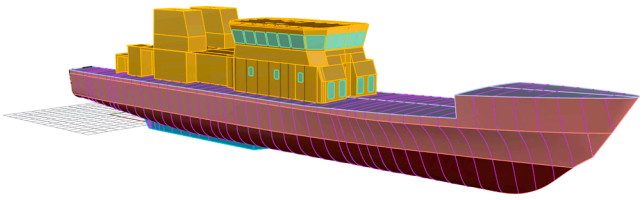

**Fig. 3.** CAD geometry of the vessel created in Rhinoceros suite.

table presents the frequency of the mode, the damping ratio, and the mode shape complexities obtained with the three estimation methods. The obtained results in terms of estimated natural frequencies are consistent between the adopted methods, thus proving the reliability of the modal identification process and confirming the robustness of the applied techniques in capturing the structural dynamics of the vessel.

## 4. Numerical modelling set-up

The following sections provide a detailed overview of the numerical model used for the analysis. First, the procedure for creating a simplified

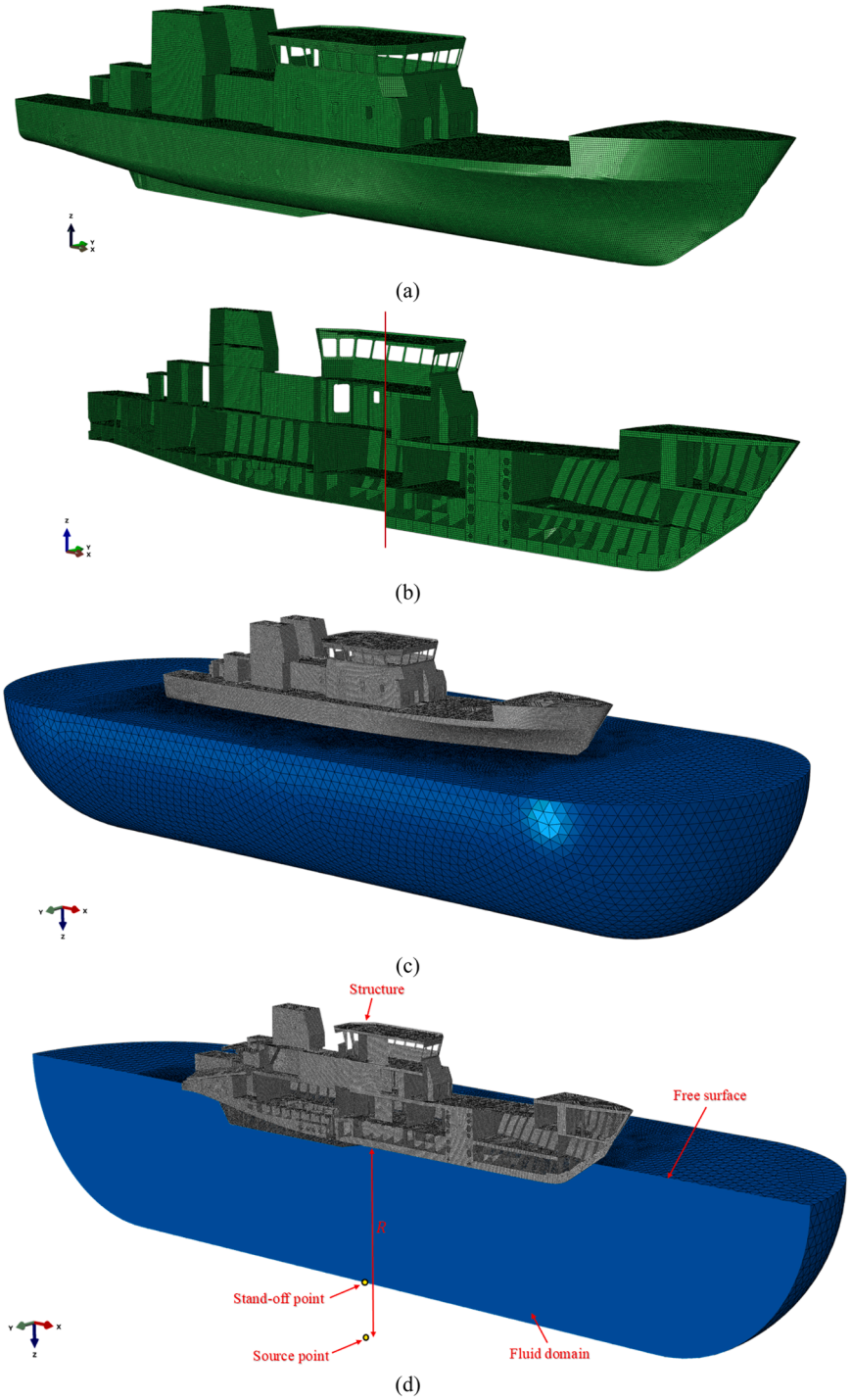


**Fig. 4.** (a) Numerical model of the ship structure, (b) internal structural arrangement, (c) global FEM model of the ship portion surrounded by the external fluid and (d) vertical section of the whole model with the identification of the domains.

**Table 4**
Material parameter used in the numerical simulation.

| $A$ [MPa] | $B$ [MPa] | $\alpha$ [-] | $C$ [-] | $\dot{\varepsilon}_0$ [$s^{-1}$] | $m$ [-] | $T_{ROOM}$ [K] | $T_M$ [K] | Ref. |
|---|---|---|---|---|---|---|---|---|
| 490 | 600 | 0.210 | 0.015 | 1.0 | 0.60 | 293 | 1800 | [59] |

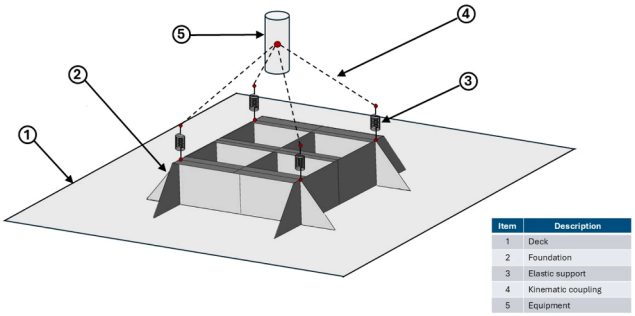


**Fig. 5.** Schematization of the subsystem composed of the foundation, resilient elements, and equipment.

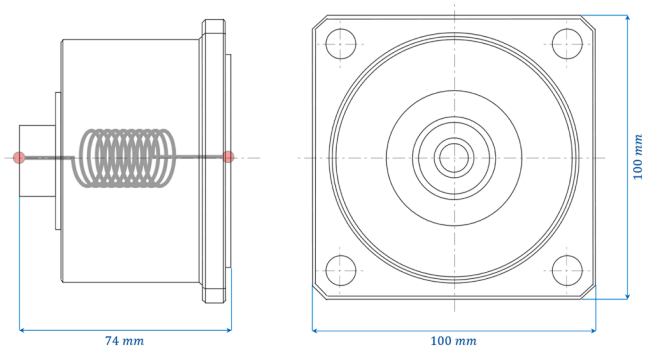


**Fig. 6.** Actual geometry of the elastic supports modelled as spring elements and inspired by the Vulkan Group's MG Series [61].

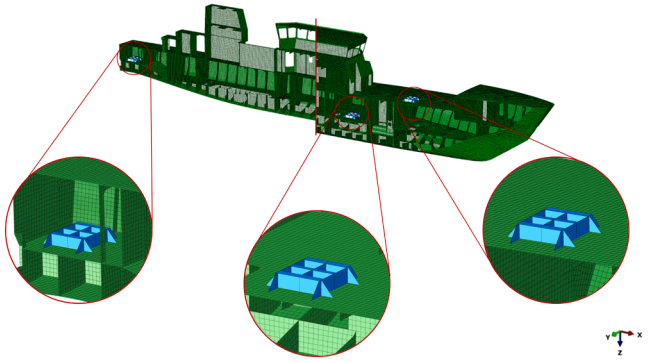

**Fig. 7.** Installation of the three foundation-resilient-equipment subsystems inside the patrol vessel.

model approximating real ship behavior is outlined. Then, the numerical model is described, including the fluid domain and meshing strategy, material parameters, boundary conditions, loading conditions, and equipment modeling. The same model, developed using the Acoustic-Structural approach in ABAQUS CAE, is used to evaluate both the dynamic response of the ship subjected to UNDEX load and ship's wetted mode shape with their related frequency, which are compared with experimental data.

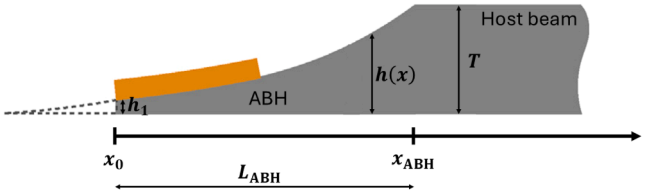


**Fig. 8.** Scheme of an ABH geometry.

### 4.1. Procedure for developing a numerical model reflecting real ship behavior

The procedure illustrated in this paragraph is conceived to develop a numerical model that accurately represents the actual conditions of the patrol vessel. The CAD model of the ship, created in Rhinoceros 8 suite, is depicted in Fig. 3.

Since precise data on the weights of the ship's internal components are unavailable, and structural details as stiffeners are not modelled, a simplified but reliable numerical model is developed using a strategy inspired by Smith's method for ship hull strength assessment and the Maestro software [54,55]. The approach is based on modeling only the plating, and assigning a uniform thickness ($t_{adjusted}$) to all surfaces of the model in Fig. 3 to consider the contribution of all the omitted detail (*e.g.*, stiffeners). Additionally, it is necessary to adjust the elastic modulus and density of the materials to restore the correct axial stiffness of the panels and the total mass of the ship, respectively.

Considering a structural mass ratio of approximately 0.3 and a total ship mass ($m_{total}$) of 4670 kN, the portion of the total mass attributed to the structure ($m_{structural}$) is approximately 1400.39 kN. Based on that, the uniform thickness value $t_{structural}$ is obtained from Eq. (6).

$$t_{structural} = \frac{m_{structural}}{A_{structural} \cdot \rho_{nom}} \tag{6}$$

where $A_{structural}$ is the total area of the surfaces of the CAD model (equal to 3167 $m^2$), while $\rho_{nom}$ is the actual density of the steel of the vessel (equal to 7750 $kg/m^3$).

The Young's modulus must be adjusted to match the normalized axial rigidity of the plates. This adjustment is applied irrespective of the plate's orientation in the ship's hull (longitudinal or transverse) and its contribution to the hull girder's overall structural response under loading. The formulation to calculate $E_{adjusted}$ is the following:

$$E_{adjusted} = \frac{E_{nom} \cdot t_{structural}}{t_{adjusted}} \tag{7}$$

where $E_{nom}$ is the actual Young's modulus of the steel (210,000 MPa), and $t_{adjusted}$ is the unknown quantity to be defined.

Finally, the density must be adjusted to ensure that the model achieves the target total mass, which includes both the structural mass and other associated masses.

$$\rho_{adjusted} = \frac{m_{total}}{A_{structural} \cdot t_{adjusted}} \tag{8}$$

where $t_{adjusted}$ is iteratively found through simulations (*i.e.*, modal analysis), and in the presented case study the value that ensures a numerical model capable of capturing the experimental natural frequencies is 0.04 m, while $A_{structural}$ and $m_{total}$ have already been defined. With this value, $E_{adjusted}$ and $\rho_{adjusted}$ are equal to 3805 $kg/m^3$ and 30,900 MPa, respectively. The modal analysis is performed using the acoustic-structural

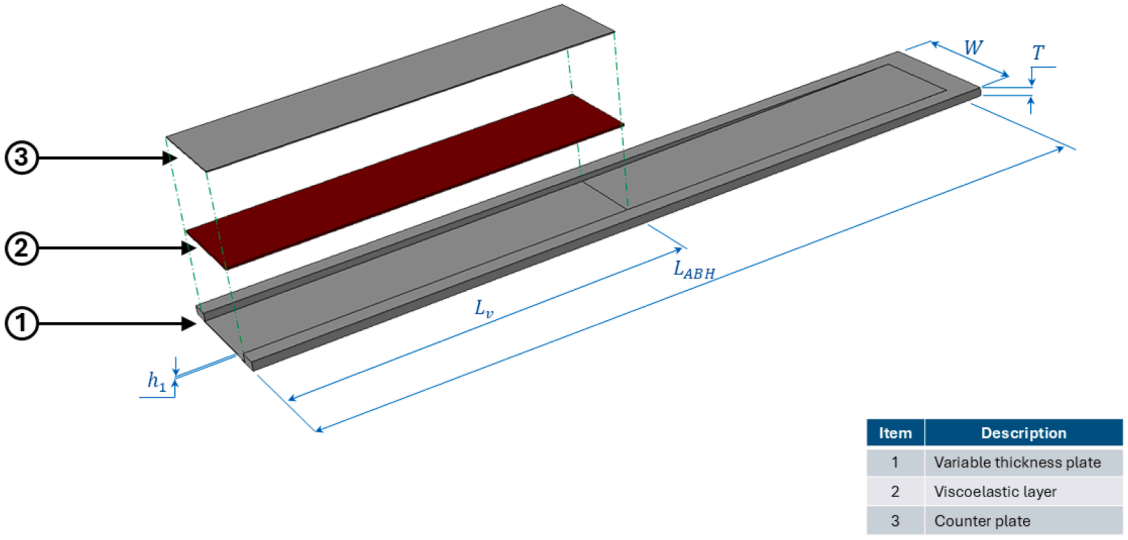


| Item | Description |
|---|---|
| 1 | Variable thickness plate |
| 2 | Viscoelastic layer |
| 3 | Counter plate |

(a)

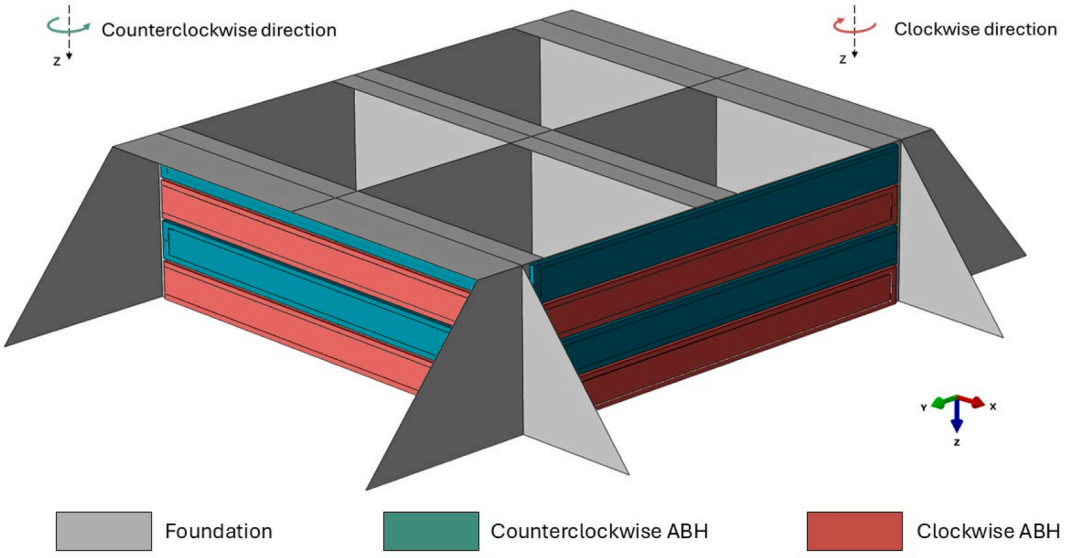


(b)

**Fig. 9.** (a) Geometry of the designed ABH (same color means same material); (b) positioning of the ABH-based metamaterial on the foundation.

**Table 5**
Geometrical parameters of the ABH.

| $W$ [mm] | $L$ [mm] | $T$ [mm] | $L_{ABH}$ [mm] | $h_1$ [mm] | $L_v$ [mm] |
|---|---|---|---|---|---|
| 70 | 880 | 10 | 850 | 1 | 440 |

**Table 6**
Mechanical characteristics of ABH materials.

| Material | $E$ [MPa] | $\nu$ [mm] | $\rho$ [kg/m$^3$] | $\eta$ [-] |
|---|---|---|---|---|
| Steel | 210,000 | 0.3 | 7800 | 0.005 |
| Viscoelastic | 5000 | 0.4 | 950 | 0.3 |

approach [56] in ABAQUS CAE by considering the water domain and, thus, calculating the wetted modes as in the real case scenario. The water domain characteristics and the mesh size, both structural and fluid, are the same as in the dynamic analysis described in the following sections.

**Table 7**
Numerical *vs* experimental natural frequencies of the vessel.

| Global mode type | Experimental frequency [Hz] | Numerical frequency [Hz] | Discrepancy [%] |
|---|---|---|---|
| 1° Vertical bending | 4.03 | 4.12 | 2.23 |
| 1° Horizontal bending | 7.40 | 7.63 | 3.11 |
| 1° Torsional | 7.87 | 8.43 | 7.12 |

Further details regarding the modal analysis are not provided, as the acoustic-structural approach used to account for the wet vibration modes of the structure is well-established in the literature [57].

The dynamic simulations are performed with ABAQUS/Explicit version 6.23, using the simplified model above described for ship

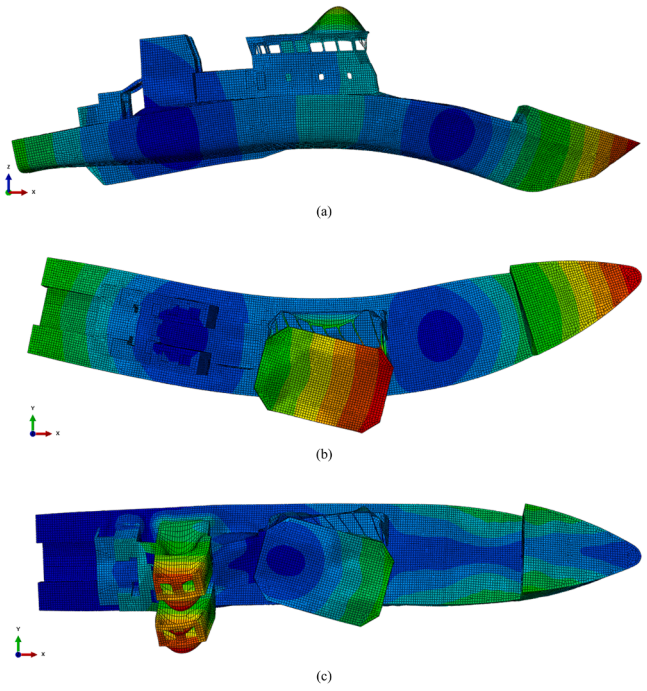


**Fig. 10.** Numerical mode shapes of the patrol vessel under investigations: (a) 1° vertical bending, (b) 1° horizontal bending and (c) 1° torsional. Acoustic domain removed for better clarity.

structures modelling.

### 4.2. Determination of fluid domain and meshing

The structural mesh base size is chosen considering 10 linear elements per bending wavelength, which can be calculated following Eq. (9) [27,58]:

$$\lambda_{bend} = \frac{c_{bend}}{f_{max}} = \sqrt{\frac{2\cdot\pi\cdot h}{f_{max}}}\sqrt{\frac{E}{12\cdot\rho\cdot(1-\nu^2)}} \tag{9}$$

where $c_{bend}$ is the speed of bending waves in the solid medium, $f_{max}$ is the maximum considered frequency (chosen equal to 150 Hz), and $h$, $E$, $\rho$ and $\nu$ are the solid characteristics, respectively thickness (equal to $t_{adjusted}$), Young's modulus (equal to $E_{adjusted}$), density (equal to $\rho_{adjusted}$) and Poisson's ratio (equal to 0.3 for steel). Thus, in the presented case study the mesh base size is equal to 0.1 m, featuring in 318,616 quadrilateral shell elements and 6072 triangular shell elements.

Fig. 4(a) and Fig. 4(b) report the employed ship meshed, including the overall geometry and the internal arrangement.

The water domain is represented in Fig. 4(c), which is discretized by 1374,293 brick elements. The size of the acoustic elements is chosen based on the smallest wavelength considered, in which ten or more linear elements must be implemented to ensure the accuracy of the results [40,45]. The fluid element length can be estimated by Eq. (10):

$$L_{max} < \frac{c}{n_{min}\cdot f_{max}} \tag{10}$$

where $L_{max}$ represents the mesh base size, $n_{min}$ the number of linear elements per smallest acoustic wavelength, $f_{max}$ the maximum frequency of interest, and $c$ the sound velocity in the acoustic medium.

In the present work, a maximum frequency of 300 Hz is considered for the UNDEX load [30] with $n_{min}$ equal to 12 and $c$ equal to 1500 m/s. Hence, $L_{max}$ should be lower than 0.96 m. To ensure sufficient solution accuracy for the acoustic pressure field near the ship and the resulting shock loading on the acoustic-structural interface, a mesh refinement is applied around the vessel. Specifically, the base size of the acoustic mesh is set around 0.8 m and a refinement of about 50 % is set near the interface between the ship and the water domain.

As regards the dimensions of the fluid domain, the standoff thickness can be considered in ABAQUS (Fig. 4(d)). The approximate radiation conditions converge to the exact condition with an infinite standoff when the thickness of the fluid domain is increased. To esteem the standoff thickness $r$ the following equation can be calculated [30]:

$$r > \frac{c\cdot m_{min}}{f_{min}} \tag{11}$$

where $m_{min}$ is a coefficient, while $f_{min}$ is the minimum considered frequency. Let assume $m_{min}$ equal to 0.33 [40,45] and $f_{min}$ equal to 35 Hz. Thus, the fluid domain thickness should be larger than 14.29 m and in the presented numerical model is set equal to 15 m. The outer boundaries of the external fluid are represented by semi-cylindrical surfaces and spherical ends. It should be noted that the values provided by the previous Eqs. (10) and (11) are recommended for analysis, although they may vary depending on other computational requirements.

### 4.3. Adopted model and boundary conditions

To evaluate the effects of UNDEX load on ship equipment, a transient analysis of the duration of 1 s is performed in ABAQUS using the acoustic-structural approach. The decision at this time is due to the intention of capturing the effects not only of the primary shock wave but also of the gas bubble, according to the indications provided later in this paragraph.

The mechanical characteristics for the ship structures are set as specified in Section 4.1. For water, the bulk modulus ($\rho_f\cdot c^2$) is equal to 2.03 GPa, and the density ($\rho_f$) is 1024 kg/m$^3$.

The plastic behavior of the ship structures is modelled using the Johnson-Cook law, with the parameters shown in Table 4, where $A$ represents the yield stress, $B$ is the strain hardening coefficient, $\alpha$ represents the hardening index, $C$ is the rate hardening coefficient, $m$ is the temperature softening coefficient, $\dot{\varepsilon}_0$ is the reference strain rate, $T_{ROOM}$ is the room temperature and finally $T_M$ is the melting temperature.

For the purposes of this paper, a material damage model for the structural steel of the ship is not implemented as the deformations are expected to remain in the elastic-plastic regime.

Because of cavitation effects (including local and bulk cavitation), the total wave formulation is employed in the transient response analysis, with the features mentioned in Section 2.

Proper non-reflecting boundary conditions are set on the boundaries of the water domain, except at the free, where a zero-relative pressure boundary condition is imposed.

The fluid-structure interaction between the water and the structure is defined at their common wet interface with a surface-based tie constraint.

### 4.4. Loading conditions

The response of the patrol vessel to the effects of a far-field UNDEX is investigated, considering both the primary shock effects and the secondary effects due to the pulsation of the gas bubble. A TNT charge having a weight $W$ equal to 516 kg is detonated 31.6 m below the water surface ($H$ parameter) with a stand-off distance $R$ (*i.e.,* the distance between the source point and the ship hull highlighted in Fig. 4(d)) equal to 28.4 m, to mimic a real torpedo attack. The explosive charge is detonated in the source point, while the UNDEX loading history is transmitted to the acoustic medium on the external boundary of the domain by specifying a reference point, as shown in Fig. 4(d). This approach is consistent with the total wave formulation algorithm, in which the incident wave loading is applied only to the outer fluid surface that separates the modeled region from the surrounding infinite acoustic

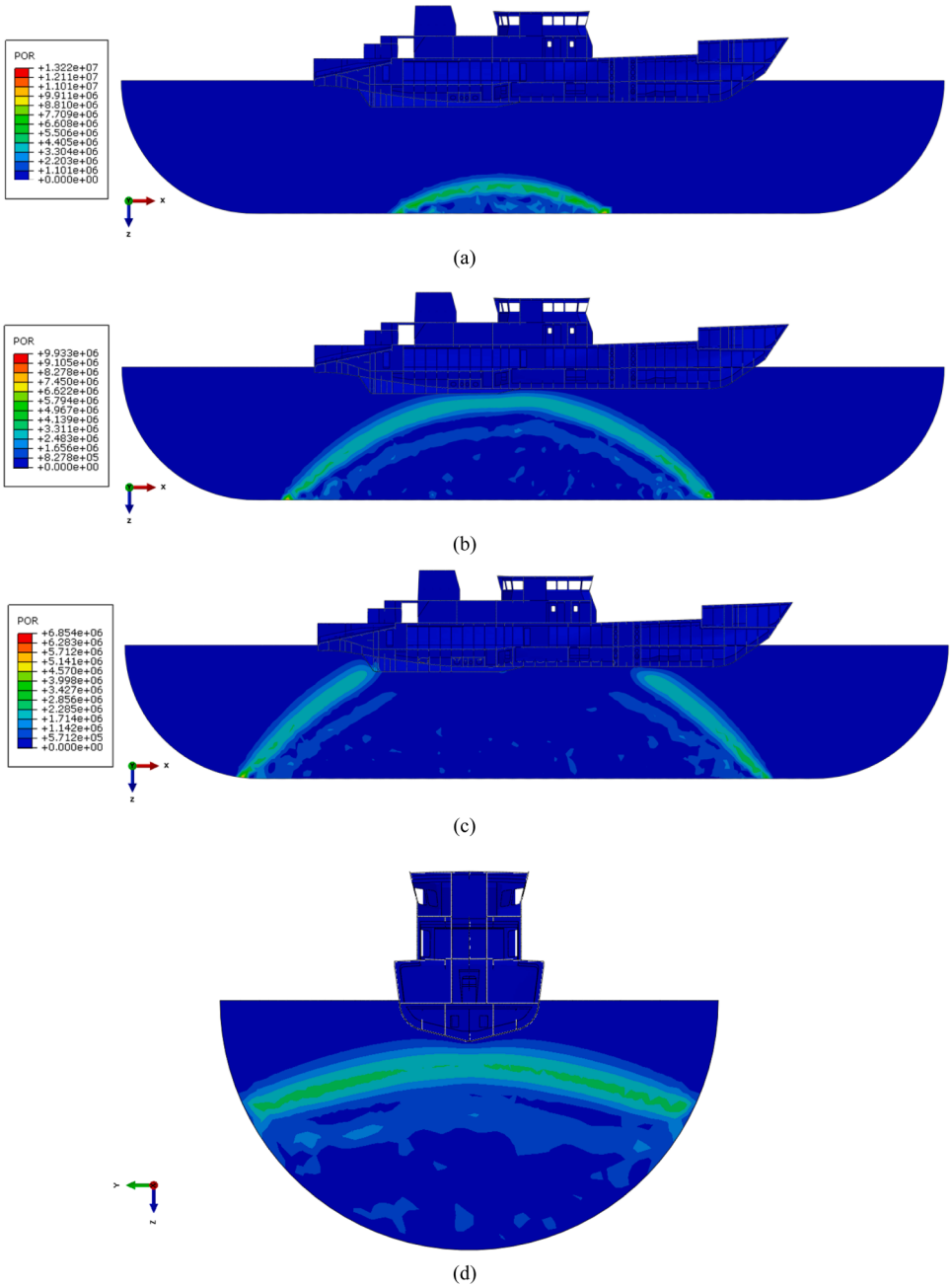


**Fig. 11.** Dynamic acoustic pressure (POR) field (in Pa) at several instants: (a) $t = 0.002$ s, (b) $t = 0.007$ s, (c) $t = 0.010$ s (longitudinal section) and (d) $t = 0.007$ s (transversal section). Legend scale adjusted for better shock front visualization.

medium. No incident wave is applied directly to the structure [43]. With this method, the loading history at the reference point is determined by the source-to-reference distance in the simulation, using the classical formulations found in the literature [9,47]. Furthermore, the effects of the gas bubble are introduced using the built-in Geers and Hunter bubble model in ABAQUS [25,42].

The pressure history of the simulated far-field UNDEX event can be approximated through Cole's empirical formulas. Eq. (8) describes the primary shock pressure with a peak $p_{max}$ and an exponential time decay, $\theta$.

$$p(t) = p_{max} \cdot e^{-\frac{t}{\theta}} \tag{8a}$$

For a TNT explosive, $p_{max}$ and $\theta$ are given by the following equations [60]:

$$p_{max} = 52.12 \cdot \left(\frac{W^{1/3}}{R}\right)^{1.18} \tag{9a}$$

$$\theta = 0.0895 \cdot W^{1/3} \cdot \left(\frac{W^{1/3}}{R}\right)^{-0.185} \tag{10a}$$

where $W$ is expressed in kg of the TNT explosive and $R$ is the stand-off distance in meters (516 kg and 28.4 m, respectively).

The calculated $p_{max}$ and $\theta$ at the stand-off distance of 28.4 m are 11.72 MPa and 0.9 ms, respectively.

As mentioned, the simulation time $t$ is set to 1 s to also capture the effects of the gas bubble. The arrival time of the secondary shock $t_a$ is estimated to be 0.771 s from the following expression:

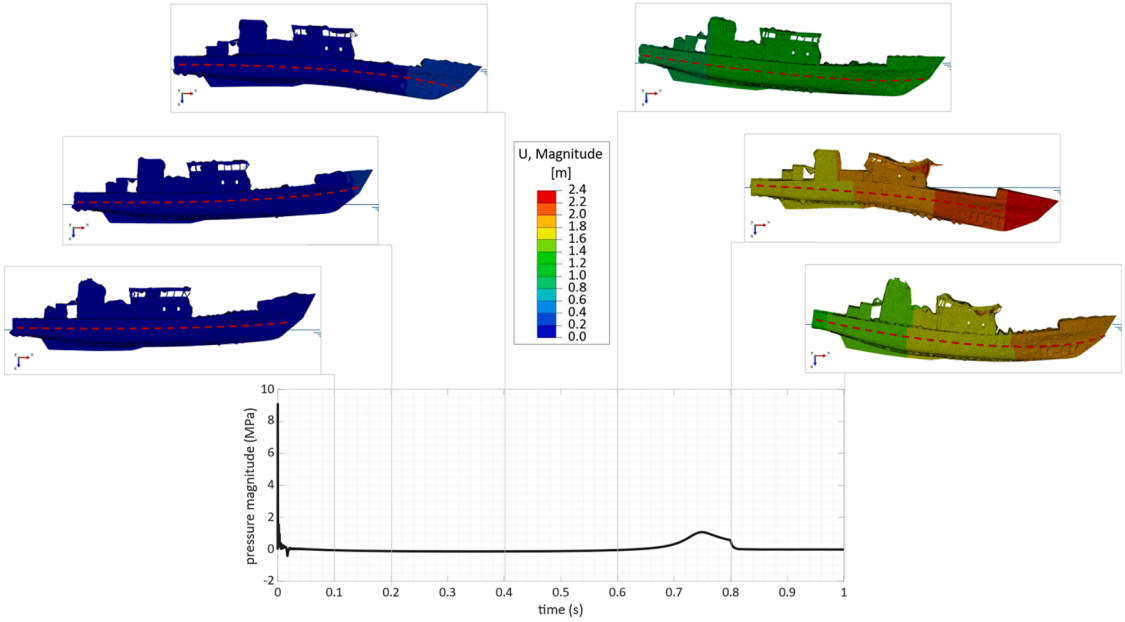


**Fig. 12.** Whipping motion of the patrol vessel and visualization of the UNDEX pressure history at the stan-off point. The displacements are magnified by a factor of 25 to enhance the visualization of global motion.

$$t_a = \frac{R}{c} + T_{bubble} \tag{11a}$$

where $T$ is the pulsation period of the gas bubble. The latter is calculated using the empirical formulation in Eq. (12), with $H$ being the depth of the explosive charge [60].

$$T_{bubble} = 2.11 \cdot \frac{W^{1/3}}{(H + 10.34)^{5/6}} \tag{12}$$

which yields a value of $T_{bubble}$ equal to 0.752 s.

### 4.5. The equipment modelling

To study the response of the equipment to the UNDEX load, a representative subsystem consisting of three elements is considered, as shown in Fig. 5. This sub-assembly is composed of: (i) the foundation, whose geometry is explicitly modelled, (ii) a resilient support corresponding to the resilient element, not explicitly modelled but represented by a spring-type connector, and (iii) the equipment, for which a representative cylindrical geometry is assumed and modelled as a point mass. This geometry was selected as representative of onboard equipment due to its comparable size, mass, and boundary conditions, which reflect typical constraints and configurations encountered in naval installations. Its simplified shape also enables efficient analysis of the main dynamic effects induced by underwater explosions.

The foundation's geometry represents a generic shipboard component foundation. It features a rectangular base measuring 1.6 $m \times 1.4$ m, including triangular brackets, with a height of 0.3 m and a thickness of 0.01 m. The four resilient mountings are modelled as a system of four parallel springs (Fig. 5). Their dimensions and elastic properties are derived from the Vulkan group's catalogue, specifically the MG series [61]. This series is chosen for its compact size, which fits within the foundation's dimensions, and for its low cut-off frequency, making it suitable for supporting various types of machinery and equipment where effective noise and vibration reduction is required.

Fig. 6 illustrates the actual geometry of the support, highlighting its spatial dimensions and the undeformed spring length, which is assumed to correspond to the total height of the support. Each spring has an axial stiffness constant of $1.5 \times 10^5$ N/m, as specified in the catalogue.

The equipment is sized according to the nominal conditions of resilient support, resulting in a cylindrical component with a mass of 270 kg. The inertial properties of the cylinder are calculated assuming it is made of steel and has a height of 0.8 m. This height is determined based on the spatial constraints of the compartments where the subassembly is installed.

To study the response of a generic component installed in different locations onboard the patrol vessel, the foundation-resilient-equipment subsystem is simultaneously installed at three different positions on the ship, as shown in Fig. 7. Following the identification of the subsystems:

- Subsystem 1 - above the double bottom at the stern of the ship;
- Subsystem 2 - on the lower deck near the arrival point of the shock load;
- Subsystem 3 - on the upper deck towards the bow.

From a numerical perspective, the foundation is modelled using shell elements with the same base size as those used for the vessel's structures. The connection between the foundation and the decks is implemented through a node-to-surface tie constraint, binding the nodes at the lower edges of the foundation to the surface of the three decks. The upper ends of the four springs are connected to the concentrated mass using kinematic coupling constraints. Additionally, since resilient supports realistically provide an elastic response only in the vertical direction, it was necessary to constrain the in-plane motion of the upper nodes of the springs. This necessity arises from the fact that spring elements in Abaqus' explicit solver cannot act in a single direction.

## 5. The acoustic black holes as a solution to vibration control

The ABH is a technique for passive vibration control that was recently developed within the structural dynamics and vibroacoustic communities. From a general perspective, the ABH effect is achieved by embedding a local thickness reduction in a thin-walled structure, typically a beam or a plate, like the one shown in Fig. 8. This thickness reduction is generated in accordance with the power law profile following reported [24,26]:

$$h(x) = \frac{T - h_1}{{L_{ABH}}^m} \cdot x^m + h_1 \tag{13}$$

where $T$ is the uniform thickness outside the ABH region, $L_{ABH}$ is the

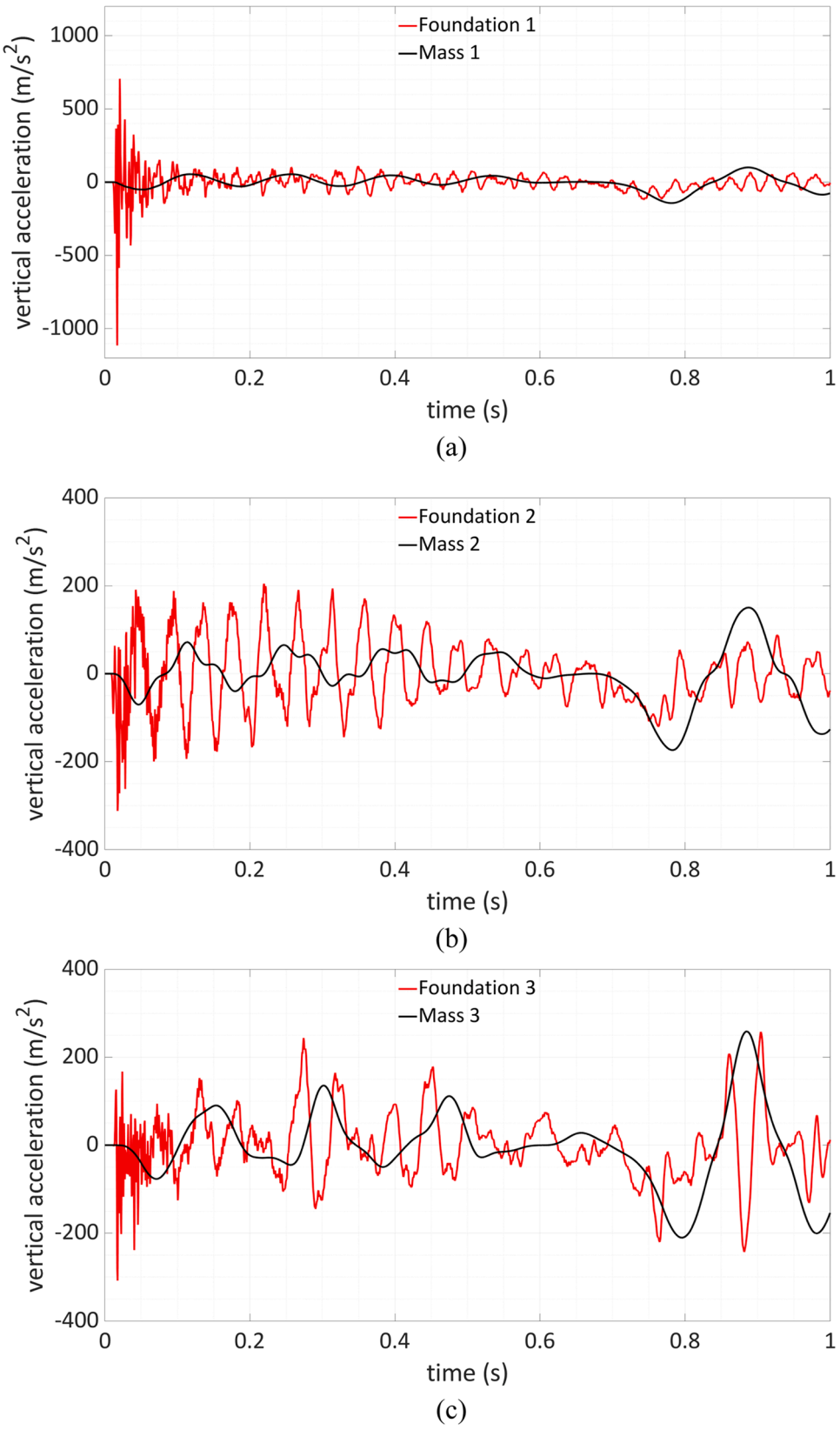


**Fig. 13.** Vertical acceleration *vs.* time plots of the three masses under study and their respective foundations accelerations: (a) mass 1, (b) mass 2 and (c) mass 3.

length of the ABH, $x$ is the generic coordinate of the variable thickness profile, $m$ is the power index (usually set as 2) and $h_1$ is the minimum thickness at the tip of the ABH.

Thanks to such power law profile, the bending waves propagating inside the structure are channeled into the ABH region where their speed experiences a smooth and continuous decrease. In the ideal case, that is

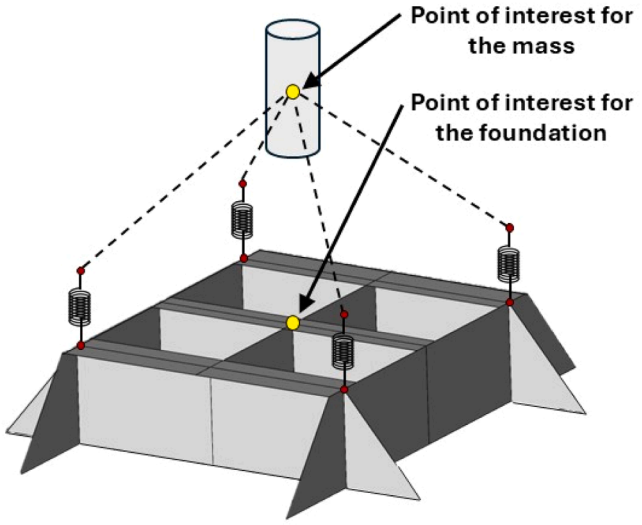


**Fig. 14.** Identification of the points of interest of the foundation–resilient–mass subsystem.

when the wall thickness vanishes at the ABH center, the wave speed decreases to zero. In the non-ideal case, that is when the ABH has a non-zero residual thickness at its center the wave speed still decreases but it never vanishes, and reflection occurs at the tip. In this latter case, which is of great importance for practical applications, a damping material (*e.g.,* viscoelastic layer) is applied to the ABH region to enhance wave energy dissipation (orange layer in Fig. 8). Thus, the ABH behaves as a wave trap that extracts vibrational energy from the host structure leading to a significant reduction in terms of both vibration and acoustic radiation [24].

Traditional embedded ABH structures, such as those described in [28,29], typically feature a very thin ABH center, making them unsuitable for load-bearing applications. To overcome this limitation, the ABH can be implemented as an external component attached to the base structure, as proposed in [62]. In this configuration, the ABH functions as a waveguide absorber (WGA) [63], directing vibrational energy away from the primary system. With appropriate damping treatment and a sufficiently long propagation path, energy reflections back into the main structure can be minimized, effectively reducing overall vibration.

The ABH is characterized by a theoretical cut-on frequency, above which its trapping effect starts. In the design stage, such frequency can be calculated with the following equation [64]:

$$f_{cut-on} = \frac{T}{2\cdot\pi\cdot {L_{ABH}}^2}\cdot\sqrt{\frac{E\cdot(40-24\cdot\nu)}{12\cdot\rho\cdot(1-\nu^2)}} \tag{14}$$

where $E$, $\nu$ and $\rho$ are respectively the Young's modulus, the Poisson's coefficient and the density of the variable-thickness portion of the ABH's material. Also, $T$ is the uniform thickness outside the ABH region and finally $L_{ABH}$ is the length of the ABH. If the vibrational waves occur at a frequency lower than such characteristic frequency of the designed ABH, they cannot be trapped into the ABH as the wavelength is bigger than the ABH length.

In this study, custom-designed ABHs are integrated into the foundation of onboard equipment using a metamaterial-inspired configuration. This approach ensures that the foundation meets structural load-bearing requirements, while the added ABHs function as vibration absorbers, mitigating the transmission of vibrations to the equipment during and after the UNDEX event. The basic ABH unit, which constitutes the unit cell of the ABH-based metamaterial, is illustrated in Fig. 9 (a). The ABH is embedded in a steel plate (Item 1) featuring a peripheral frame that allows it to be welded to the host structure (*i.e.*, the equipment foundation). To enhance damping performance and promote vibrational energy dissipation, a constrained viscoelastic layer (2 mm, Item 2) is applied in the ABH region, topped with a 1 mm counter plate (Item 3).

The ABH-based metamaterial is composed of 16 ABHs, arranged in pairs and mounted on the four side walls of the equipment foundation. Within each pair, one ABH is oriented clockwise and the other counterclockwise, meaning they have opposite variable-thickness profiles. Specifically, a "clockwise" orientation refers to a thickness that decreases in a clockwise direction when viewed from above, relative to the global Z-axis of the structure; conversely, a "counterclockwise" orientation exhibits the opposite trend (Fig. 9(b)).

Compared to conventional ABH absorbers proposed in [62,65], which interface with the host structure through only one or a few coupling points, the additive ABHs presented in this study are connected along their entire perimeter, resulting in multiple coupling interfaces. This configuration significantly improves the efficiency of energy transfer from the base structure to the ABHs. A critical factor in the effective performance of ABHs lies in their placement, which should coincide with regions of high vibrational energy concentration [20,22]. In general, ABHs must be positioned where vibrational energy is most intense [66], a requirement that is difficult to satisfy with traditional added-ABH configurations [62], due to their limited interface with the host structure. By contrast, the proposed ABHs with continuous perimeter coupling overcome this limitation, enabling vibrational energy to be efficiently channeled into the ABH from all directions.

The choice to place the ABHs along the side walls of the foundation is based on the analysis of energy transmission pathways from the hull to the onboard equipment. Following the impact of the primary shock wave, vibrational energy spreads through the structural components of the ship, with the foundation side walls acting as critical transfer elements. The ABHs are mounted horizontally to the host structure, a configuration that not only conserves space but also maximizes the available ABH length—an important parameter influencing the cut-on frequency.

The number of ABH absorbers is dictated by the available space. It was observed that the thinner the ABH, the greater their effectiveness. Therefore, 4 ABH per side represents the optimal compromise between high effectiveness of the ABH-based metamaterial and the constructive limitations imposed by their manufacturing processes. Regarding their orientation, the alternation between clockwise and counterclockwise ABH is chosen with the aims to optimize the absorption of vibrational energy. If all ABH are oriented in the same direction, a vertical channel would be created, allowing vibrational energy to pass through undisturbed, thus reducing the system's effectiveness. It's important to note that the ABH are not in direct contact with the main structure at their tip.

The geometrical parameters of the proposed ABH are reported in Table 5, where $W$ and $L$ are respectively the width and length of the steel plate, $L_v$ is the length of the constrained viscoelastic material and finally $T$, $L_{ABH}$ and $h_1$ have been already defined previously. As previously explained, the ABH length $L_{ABH}$ is dictated by the available space, and the cut-on frequency of the single ABH is around 19.91 Hz. To notice is that in the available literature the ABHs are applied as solution to reduce vibration and noise in the medium-high frequency range, while they use at low frequency is challenging as lower is the cut-on frequency and higher are the ABH's dimensions [67].

The mechanical characteristics of the materials are reported in Table 6, where $\eta$ represents the loss factor, while the definition of the other parameters is well known.

## 6. Results and discussion

In the following sections, the comparison between the experimental and calculated wet modes of the ship is presented to assess the accuracy of the adopted numerical model. Then, the structural response of the whole ship is addressed, and finally the vibrations on both the

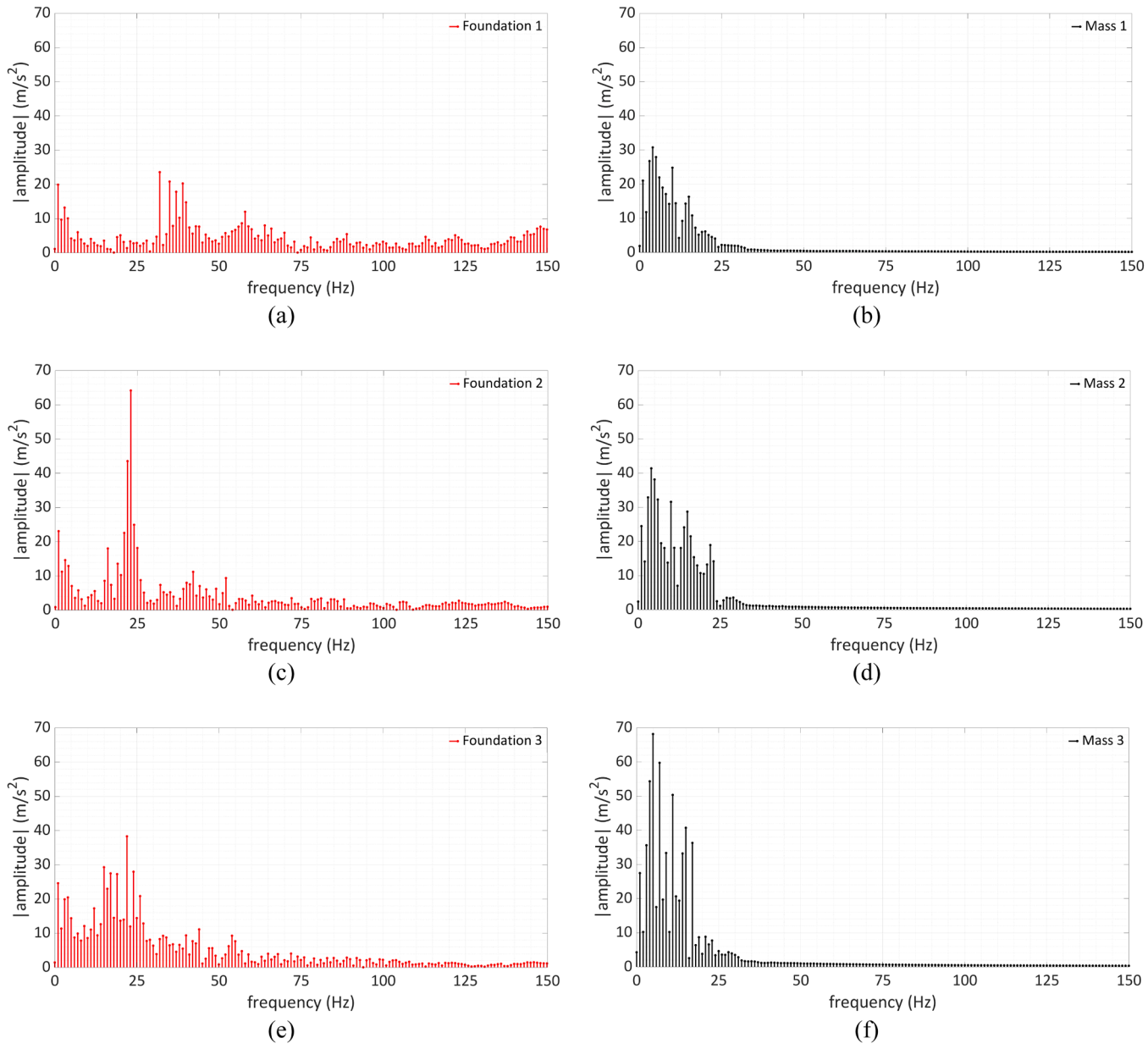


**Fig. 15.** FRF of the three masses and their respective foundations without ABH: (a) foundation 1, (b) mass 1, (c) foundation 2, (d) mass 2, (e) foundation 3 and (f) mass 3. Same range of values on the x-axis and y-axis.

foundation and the connected mass are evaluated to show the effectiveness of the ABH-based metamaterial in reducing the vibration of the mounted equipment.

### 6.1. Numerical calculation of the wet modes of the vessel

Table 7 presents a comparison between the natural frequencies of the vessel numerically obtained and those experimentally measured. The experimental values used as reference for the comparison were derived using the EFDD method (see Section 3). The discrepancies between the obtained results are about 2.23 %, 3.11 %, and 7.12 % for the first vertical bending, horizontal bending, and torsional modes, respectively, highlighting a good correlation between the numerical and experimental results. The numerical predictions slightly overestimate the experimental values, especially for the torsional mode. However, these differences remain lower than 10 %, confirming the reliability of the adopted numerical model. Fig. 10 illustrates the mode shapes associated with the frequencies reported in Table 7.

### 6.2. Global dynamic response of the vessel

The simulations performed to evaluate the dynamic response of the vessel require approximately 72 h for a workstation with 128 GB of RAM and an Intel® CoreTM i9–14,900 K 3.20 GHz CPU.

Fig. 11 documents the progression of the primary shock front within the acoustic domain at three successive representative time instants, showing the dynamic acoustic pressure (POR) in both longitudinal and transversal sections.

The POR time history extracted at the stand-off point (depicted in Fig. 4(d)) is presented in Fig. 12. It is characterized by an initial pressure peak of 9.4 MPa caused by the primary shock, followed by an exponential decay. A second peak appears at approximately 0.75 s due to the gas bubble pulsation. This secondary pressure pulse has a lower magnitude but extends over a longer time window. The arrival time is close to the empirical estimate from Eq. (11) (0.771 s), with a 2.8 % difference attributable to the simplified nature of the empirical formula compared to the more detailed coupled simulation.

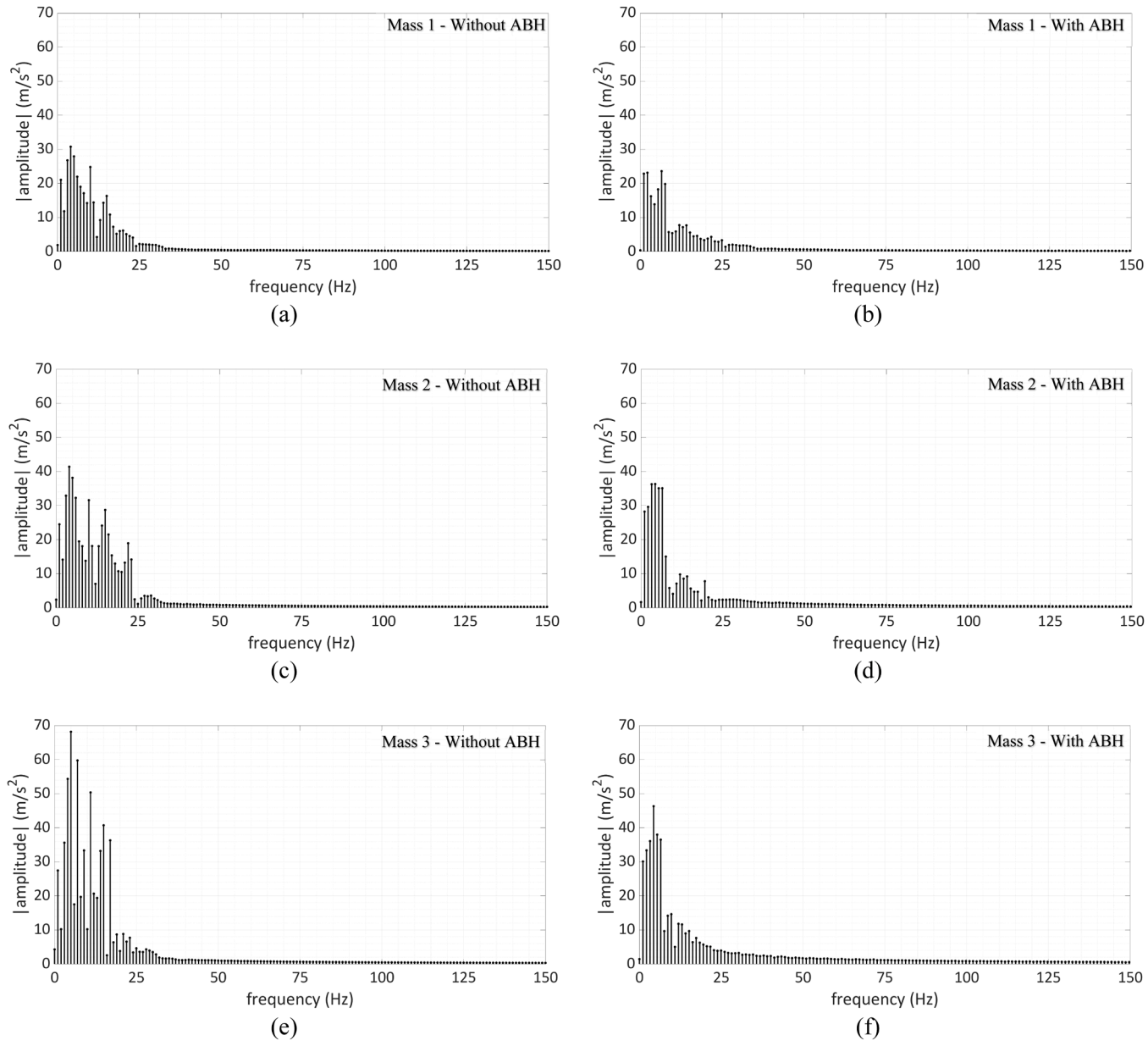


**Fig. 16.** FRF of the three masses with and without the effects of the ABH-based metamaterial pattern: (a) mass1, (b) mass 1 - ABH, (c) mass 2, (d) mass 2 - ABH, (e) mass 3 and (f) mass 3 - ABH. Same range of values on the x-axis and y-axis.

The global response of the patrol vessel in terms of displacement at key instants is detailed in Fig. 12. The development of the whipping motion can be highlighted, and the hogging and sagging deformation can be qualitatively appreciated.

### 6.3. *Dynamic response of the equipment with traditional resilient mounting*

The vertical accelerations calculated in time domain for the traditional mounting (*i.e.*, foundation, resilient mounting and equipment) are reported in Fig. 13. Specifically, a comparison between the accelerations recorded on the mass (in black) and at the central point of the upper surface of the foundation (in red) is made for each foundation. The control locations are highlighted in Fig. 14 for better comprehension. The dynamic response of the foundation-resilient-mass subsystems subjected to an UNDEX event is characterized by three distinct phases: an initial sharp peak corresponding to the arrival of the UNDEX primary shock, a subsequent phase of oscillations, and a third phase, which starts around 0.8 s, marked by the arrival of the first pulsation of the gas bubble.

A close examination of Fig. 13 highlights the differences in accelerations generated both in the foundation and in the overlying mass, depending on the system's positioning onboard the ship. This variation is influenced not only by the global dynamics of the vessel but also by the propagation of vibrational energy through the structures. The intensity and speed of this energy transmission can be affected by factors such as structural thickness, the presence of damping materials, and preferential energy flow paths.

Additionally, a notable difference is observed between the accelerations of the foundation and those of the overlying mass. The former exhibits more pronounced peaks, while the latter experiences a smoother, damped response because of the resilient mount. This damping of acceleration amplitudes is crucial for protecting the component and ensuring its functionality. Furthermore, the presence of the resilient mount introduces a significant shift between the two responses.

To evaluate the effectiveness of the equipment supports, it is also useful to evaluate the frequency contribution of the dynamic responses, to better design the damping solutions. As a matter of fact, they are usually characterized by a cut-off frequency. The higher frequencies are damped, while the lower ones are amplified.

To identify the frequency content of the signals presented in Fig. 13 and to understand the frequencies filtered out by the traditional solution (Vulkan supports), a Fast Fourier Transform (FFT) is performed on the different acceleration signals using the built-in function in MatLab. The FFT is carried out using a time step $\Delta t$ of 0.0001 s and a sampling frequency $f_s$ of 10,000 Hz.

The results of the FFT are presented in Fig. 15, considering a frequency range from 0 to 150 Hz, consistent with the maximum frequency limits imposed by Eq. (9). The amplitude spectrums of the acceleration signals of Fig. 15 are computed considering a normalization factor of $2/N$ (with $N$ number of samples of the signal) to preserve physical consistency, while the horizontal axis shows the frequency in Hz.

Fig. 15 highlights the differences in the frequency response function (FRF) of the foundations and the masses. Specifically, all the foundations exhibit a response with a broadband spectrum. The peaks with higher amplitudes up to 65 m/s$^2$ are in the interval 10–50 Hz (Fig. 15(a), (c) and (e)). Regarding the masses, as shown in Fig. 15(b), (d) and (f), they show a significantly dampened response, especially above 35 Hz. Starting from this frequency (characteristic frequency), the resilient mountings effectively filter out higher-frequency excitations, leading to a marked reduction in amplitude, with peak values reduced to approximately 20 m/s$^2$. This behavior is in line with the information available inside the Vulkan datasheet correspondent to the MG series support [61], further supporting the accuracy and reliability of the obtained numerical results.

Despite that, peaks with amplitudes up to 70 m/s$^2$ are evaluated in the intervals of 1–30 Hz, especially for the subsystem located on the upper deck towards the bow.

All these considerations highlight the effectiveness of the resilient mountings (*e.g.*, Vulkan supports) in attenuating medium-high frequency vibrations. However, as expected, their contribution is less effective in the low-frequency range, where vibrational isolation becomes more challenging due to the intrinsic dynamic behavior of such passive systems.

### 6.4. Dynamic response of the equipment with traditional mounting combined with the ABH-based metamaterial pattern

To evaluate the effectiveness of the designed ABH-based metamaterial in enhancing the vibration reduction of the equipment, the FRF of the modelled mass is evaluated and compared with the one calculated for the traditional solution (Fig. 16).

The effect of the ABH-based metamaterial is clearly visible starting approximately from 20 Hz. The proposed solution reduces up to 20 m/s$^2$ the amplitude of the FRF in the range 10–30 Hz where the traditional solution is not effective. Furthermore, although there are still peaks in the lower frequencies, their amplitudes are reduced by about 5–10 m/s$^2$.

The results obtained are not only in line with the analytical design of the system but highlight its potential in increasing vibration control. This opens the possibility of future studies that include the optimization of the ABH component itself, and the foundation. The aim of such a study should be the maximization of the available spaces, and the minimization of the overall dimensions of the ABH unit. This will allow the design of the ABH component with a lower cut-on frequency, extending the operating range through lower frequency. Moreover, the effectiveness of the ABH-based pattern could be further increased by optimizing the positioning of the unit cell and their number.

## 7. Conclusions

The dynamic response of marine structures subjected to underwater explosions (UNDEX) represents a critical challenge for ensuring operational safety and structural integrity, particularly in non-contact scenarios. The shock waves and bubble oscillations generated by UNDEX events induce vibrations that propagate through the hull, negatively affecting onboard equipment and compromising its performance. Traditional resilient mountings are commonly employed to mitigate these effects. However, their effectiveness is often limited by design constraints, including stiffness, target frequency range, and equipment mass. The frequency range of the induced vibrations and their coupling with the equipment are difficult to estimate, especially in the early design stage.

To address these limitations, a high-fidelity modeling approach is proposed to evaluate the dynamic behavior of representative onboard equipment. Specifically, the application of an acoustic black hole (ABH)-based metamaterial pattern is explored to enhance the vibration reduction achieved by traditional resilient mountings.

A patrol vessel is selected as the reference military ship for this investigation. The numerical model used for the UNDEX simulations is validated against experimental data, using the ship's natural frequencies as a reference parameter. A subsystem, composed of a generic foundation, resilient mountings, and a mass representative of the onboard equipment, is placed in three different locations along the ship.

The first objective of this study is to evaluate the frequency response function (FRF) of both the foundation and the equipment mounted with traditional resilient mountings when the vessel is subjected to a non-contact UNDEX event. Subsequently, the effectiveness of an ABH-based metamaterial in enhancing vibration control performance is assessed.

The results demonstrate the feasibility of the designed ABH-based metamaterial, leading to a significant reduction in FRF amplitude (up to 20 m/s$^2$). Specifically, the introduction of ABH results in an average peak amplitude reduction of approximately 61 %, when compared to traditional resilient mountings alone. This combined configuration significantly attenuates the dynamic response between the foundation and the mounted mass, providing an effective damping solution—well aligned with the vibration isolation targets commonly adopted in the naval sector (typically around 80 %).

These findings highlight the potential of ABH-based metamaterials to enhance the protection of onboard equipment in naval vessels subjected to UNDEX events. Future studies will further optimize both the ABH unit cell and the ABH-based metamaterial pattern and positioning to maximize their effectiveness.

Beyond the immediate application to naval platforms, the long-term impact of this research lies in the advancement of passive vibration control strategies through geometry-based solutions that are lightweight, scalable, and compatible with existing manufacturing technologies. The proposed methodology enhances survivability and mission readiness by improving the protection of critical equipment from high-intensity vibrational loads. Moreover, its applicability extends to other sectors where structural reliability under dynamic excitation is crucial, such as offshore platforms, subsea vehicles, and marine energy systems. Potential benefits also exist in aerospace and automotive fields, where compact and efficient damping solutions are increasingly needed. Finally, the development of a high-fidelity simulation framework based on a validated acoustic-structural approach supports a simulation-driven design workflow, which aligns with the growing trend toward digital engineering in the naval and structural design industries.

While the results are promising, some limitations should be acknowledged. First, the practical implementation of ABH-based components may be constrained by manufacturing challenges, as producing thin-walled structures with gradual thickness variation, especially down to very small residual values, can be both technically demanding and costly. Second, the present study relies exclusively on numerical simulations and experimental validation is still required to confirm the practical effectiveness of the proposed solution. Moreover, the ABH geometry and its integration within the mounting system were not

optimized, as the current configuration was designed based on general criteria and available space. Future work should address both experimental testing and geometry optimization under realistic manufacturing and installation constraints.

*Data availability statement*

The data given in this article and the data supporting the results of this study are not available.

## CRediT authorship contribution statement

**Jacopo Bardiani:** Writing – review & editing, Writing – original draft, Visualization, Validation, Methodology, Investigation, Formal analysis, Data curation, Conceptualization. **Giada Kyaw Oo D'Amore:** Writing – review & editing, Writing – original draft, Validation, Methodology, Investigation, Formal analysis, Data curation, Conceptualization. **Giovanni Marchesi:** Writing – review & editing, Writing – original draft, Methodology, Formal analysis, Data curation, Conceptualization. **Marco Biot:** Writing – review & editing, Supervision, Resources, Methodology. **Claudio Sbarufatti:** Writing – review & editing, Supervision, Resources, Methodology. **Andrea Manes:** Writing – review & editing, Supervision, Resources, Methodology, Conceptualization.

## Declaration of competing interest

The authors declare that they have no known competing financial interests or personal relationships that could have appeared to influence the work reported in this paper.

## Acknowledgements

This project has received funding from the European Defence Fund (EDF) under grant agreement 101103257 dTHOR — EDF-2021-NAVAL-R-2.

Also, the author would like to thank SAAB company for providing a good approximation numerical model of the KBV 201 vessel and the Swedish Coastguard who owns and operates the ships.

## Data availability

The authors do not have permission to share data.

## References

[1] A. Sarhadi, M. Ravanshadnia, A. Monirabbasi, M. Ghanbari, Using an improved U-Net++ with a T-max-Avg-pooling layer as a rapid approach for concrete crack detection, Front. Built Environ. 10 (2024), https://doi.org/10.3389/fbuil.2024.1485774.

[2] A. Sarhadi, M. Ravanshadnia, A. Monirabbasi, M. Ghanbari, Optimizing concrete crack detection: an attention-based Swin U-Net approach, IEEE Access 12 (2024) 77575–77585, https://doi.org/10.1109/ACCESS.2024.3403389.

[3] A. Sarhadi, M. Ravanshadnia, A. Monirabbasi, M. Ghanbari, An innovative dense RESU-NET architecture with T-max-avg pooling for advanced crack detection in concrete structures, IEEE Open J. Comput. Soc. (2024), https://doi.org/10.1109/OJCS.2024.3481000.

[4] J. Bardiani, C. Sbarufatti, A. Manes, Transfer learning with deep neural network toward the prediction of the mass of the charge in underwater explosion events, J. Mar. Sci. Eng. 13 (2025) 190, https://doi.org/10.3390/jmse13020190.

[5] J. Bardiani, M. Giglio, C. Sbarufatti, A. Manes, On the Exploration of the Influence of Seabed Reflected Waves on Naval Structures, AIAS 2024, Basel Switzerland: MDPI, 2025, p. 7, https://doi.org/10.3390/engproc2025085007.

[6] J. Bardiani, L. Lomazzi, C. Sbarufatti, A. Manes, A machine learning-based tool to correlate coupled and uncoupled numerical simulations for submerged plates subjected to underwater explosions, J. Mar. Sci. Appl. (2025), https://doi.org/10.1007/s11804-025-00624-5.

[7] Y.G. dong, F. Y, W.G. hui, C.X. ze, L.Z. dong, LuW bo, Blast resistance of air-backed RC slab against underwater contact explosion, Def. Technol. 28 (2023) 236–250, https://doi.org/10.1016/j.dt.2022.11.004.

[8] J. Liu, AnF jiang, C. Wu, L.S. sha, Z.M. xue, X.D. yu, et al., Experimental investigations on small-and full-scale ship models with polyurea coatings subjected to underwater explosion, Def. Technol. 18 (2022) 1257–1268, https://doi.org/10.1016/j.dt.2021.05.011.

[9] R.H. Cole, R. Weller, Underwater explosions, Phys. Today 1 (1948), https://doi.org/10.1063/1.3066176, 35–35.

[10] Z. Aman, Z. Weixing, W. Shiping, F. Linhan, Dynamic response of the non-contact underwater explosions on naval equipment, Mar. Struct. 24 (2011) 396–411, https://doi.org/10.1016/j.marstruc.2011.05.005.

[11] LiH tao, Z.X. ying, C. Zhang, M.Z. yuan, B.X. fei, K. Liu, Sagging damage characteristics of hull girder with trapezoidal cross-section subjected to near-field underwater explosion, Def. Technol. 21 (2023) 1–13, https://doi.org/10.1016/j.dt.2021.10.004.

[12] J. Liu, AnF jiang, C. Wu, L.S. sha, Z.M. xue, X.D. yu, The early responses of air-backed plate subjected to underwater explosion with aluminized explosives, Def. Technol. 16 (2020) 642–650, https://doi.org/10.1016/j.dt.2019.11.003.

[13] P. Tran, C. Wu, M. Saleh, L. Bortolan Neto, H. Nguyen-Xuan, A.J.M Ferreira, Composite structures subjected to underwater explosive loadings: a comprehensive review, Compos. Struct. 263 (2021), https://doi.org/10.1016/j.compstruct.2021.113684.

[14] F.R. Ming, A.M. Zhang, Y.Z. Xue, S.P. Wang, Damage characteristics of ship structures subjected to shockwaves of underwater contact explosions, Ocean Eng. 117 (2016) 359–382, https://doi.org/10.1016/j.oceaneng.2016.03.040.

[15] F.V. de Camargo, Survey on experimental and numerical approaches to model underwater explosions, J. Mar. Sci. Eng. 7 (2019), https://doi.org/10.3390/jmse7010015.

[16] Z.F. Zhang, C. Wang, L.K. Wang, A.M. Zhang, V.V Silberschmidt, Underwater explosion of cylindrical charge near plates: analysis of pressure characteristics and cavitation effects, Int. J. Impact Eng. 121 (2018) 91–105, https://doi.org/10.1016/j.ijimpeng.2018.06.009.

[17] J.M. Didoszak, Y.W. Kwon, Failure assessment of shipboard equipment subjected to underwater explosions, Multiscale Multidisc. Model. Experim. Design 8 (2025), https://doi.org/10.1007/s41939-024-00637-7.

[18] J. Bardiani, C. Mazzolatti, A. Manes, C. Sbarufatti, A hybrid approach to enhance decision-making in marine structures: combining sensor data with human perception, Results Eng. 105670 (2025), https://doi.org/10.1016/j.rineng.2025.105670.

[19] J.Y. Du, Z.P. Du, Y. Li, K. Shao The progress of naval ship explosion protection technology 2015(36):391–400.

[20] J.C. Ji, Q. Luo, K. Ye, Vibration control based metamaterials and origami structures: a state-of-the-art review, Mech. Syst. Signal. Process. 161 (2021), https://doi.org/10.1016/j.ymssp.2021.107945.

[21] M.R. Machado, M. Dutkiewicz, G.B. Colherinhas, Metamaterial-based vibration control for offshore wind turbines operating under multiple hazard excitation forces, Renew Energy 223 (2024), https://doi.org/10.1016/j.renene.2024.120056.

[22] S. Dalela, P.S. Balaji, D.P. Jena, A review on application of mechanical metamaterials for vibration control, Mech. Adv. Mater. Struct. 29 (2022) 3237–3262, https://doi.org/10.1080/15376494.2021.1892244.

[23] W. Liu, L. Wu, J. Zhang, J. Sun, J. Zhou, Metamaterial springs for low-frequency vibration isolation, J. Materiomics 11 (2025), https://doi.org/10.1016/j.jmat.2024.04.009.

[24] A. Pelat, F. Gautier, S.C. Conlon, F. Semperlotti, The acoustic black hole: a review of theory and applications, J. Sound Vib. 476 (2020), https://doi.org/10.1016/j.jsv.2020.115316.

[25] V. Krylov, Acoustic black holes: recent developments in the theory and applications, Ultrasonics Ferroelectr. Freq. Control IEEE Trans. 61 (2014) 1296–1306, https://doi.org/10.1109/TUFFC.2014.3036.

[26] C. Zhao, M.G. Prasad, Acoustic black holes in structural design for vibration and noise control, Acoustics 1 (2019) 220–251, https://doi.org/10.3390/acoustics1010014.

[27] E.P. Bowyer, V. Krylov A review of experimental investigations into the acoustic black hole effect and its applications for reduction of flexural vibrations and structure-borne sound, 2015.

[28] J. Deng, N. Gao, X. Chen, H. Pu, J. Guo, Underwater sound radiation from a Mindlin plate with an acoustic black hole, Ocean Eng. 278 (2023) 114376, https://doi.org/10.1016/j.oceaneng.2023.114376.

[29] S. Gao, Z. Tao, Y. Li, F. Pang, Application research of acoustic black hole in floating raft vibration isolation system, Rev. Adv. Mater. Sci. 61 (1) (2022) 888–900, https://doi.org/10.1515/rams-2022-0235.

[30] L. Ge, A.M. Zhang, S.P. Wang, Investigation of underwater explosion near composite structures using a combined RKDG-FEM approach, J. Comput. Phys. 404 (2020), https://doi.org/10.1016/j.jcp.2019.109113.

[31] C. Widanage, D. Mohotti, C.K. Lee, D.P.P. Meddage, K. Wijesooriya, Explainable machine learning-based prediction of blast loads on structural surfaces in two-dimensional spatial coordinates, Results Eng. 26 (2025) 104979, https://doi.org/10.1016/j.rineng.2025.104979.

[32] Z. Tokmechi, A. Davoudi-Kia, Investigation of the probability of RCC dams' failure due to the blast loading by using the Monte Carlo method, Results Eng. 26 (2025) 105293, https://doi.org/10.1016/j.rineng.2025.105293.

[33] S. Peyman, A. Eskandari, Analytical and numerical study of concrete slabs reinforced by steel rebars and perforated steel plates under blast loading, Results Eng. 19 (2023) 101319, https://doi.org/10.1016/j.rineng.2023.101319.

[34] K. Zhang, X. Li, Y. Peng, F. Lu, Z. Tian, Failure similarity of gravity dam under downstream contacting blast loading, Results Eng. 21 (2024) 101848, https://doi.org/10.1016/j.rineng.2024.101848.

[35] A. Pintilie, M.G. Manea, D. Mărășescu, O. Cristea, P. Burlacu, C.P. Clinci, N.S. Popa, Optimization of bulk carrier hull design through cad modelling and fem structural

analysis – a case study, Results Eng. 26 (2025) 104846, https://doi.org/10.1016/j.rineng.2025.104846.
[36] Y. Zuo, W. Fu, P. Xu, X. Wang, S. Li, S. Xu, H. Wu, Y. Liu, J. Xiao, H. Wang, Study on vibration characteristics of large caliber naval gun cradle based on similarity theory, Results Eng. 15 (2022) 100529, https://doi.org/10.1016/j.rineng.2022.100529.
[37] Y.Z. Liu, S.F. Ren, P.F. Zhao, Application of the deep neural network to predict dynamic responses of stiffened plates subjected to near-field underwater explosion, Ocean Eng. 247 (2022), https://doi.org/10.1016/j.oceaneng.2022.110537.
[38] K.X. shao, G. H, Z. Jin, C. Zheng, Y. Wang, Predictions of the responses of stiffened plates subjected to underwater explosion based on machine learning, Ocean Eng. 283 (2023), https://doi.org/10.1016/j.oceaneng.2023.115216.
[39] R. Löhner, L. Li, O.A. Soto, J.D. Baum, An arbitrary lagrangian–Eulerian method for fluid–structure interactions due to underwater explosions, Int. J. Numer. Methods Heat Fluid Flow 33 (2023) 2308–2349, https://doi.org/10.1108/HFF-08-2022-0502.
[40] Q.L. Zhang, X.Y. Huang, Z. Li, Coupled acoustic-structural analysis of a partially submerged circular rc column in an underwater explosion event: factors to be considered for loading, Ocean Eng. 232 (2021), https://doi.org/10.1016/j.oceaneng.2021.109122.
[41] F. den Abeele, P. Verleysen, Finite element analysis of subsea pipelines subjected to underwater explosion, in: Proceedings of the International Conference On Offshore Mechanics and Arctic Engineering - OMAE 2, 2013, https://doi.org/10.1115/OMAE2013-10736.
[42] C.Y. Jen, Coupled acoustic-structural response of optimized ring-stiffened hull for scaled down submerged vehicle subject to underwater explosion, Theor. Appl. Fract. Mech. 52 (2009) 96–110, https://doi.org/10.1016/j.tafmec.2009.08.006.
[43] J. Qiankun, D. Gangyi, A finite element analysis of ship sections subjected to underwater explosion, Int. J. Impact Eng. 38 (2011) 558–566, https://doi.org/10.1016/j.ijimpeng.2010.11.005.
[44] A.J. Moradloo, A. Adib, A. Pirooznia, Damage analysis of arch concrete dams subjected to underwater explosion, Appl. Math. Model. 75 (2019) 709–734, https://doi.org/10.1016/j.apm.2019.04.064.
[45] M. Smith, ABAQUS/Standard User's Manual, Version 6, 9, Dassault Systèmes Simulia Corp, United States, 2009.
[46] Y.W. Kwon, P.K. Fox, Underwater shock response of a cylinder subjected to a side-on explosion, Comput. Struct. 48 (4) (1993) 637–646.
[47] B.V. Zamyshlyayev, Y.S. Yakovlev. Dynamic loads in underwater explosion. Washington, DC, USA 1973.
[48] Y. Wang, H. Dong, T. Dong, X. Xu, Dumbbell-shaped damage effect of closed cylindrical shell subjected to far-field side-on underwater explosion shock wave, J. Mar. Sci. Eng. 10 (2022), https://doi.org/10.3390/jmse10121874.
[49] Z. Zong, Y. Zhao, H. Li, A numerical study of whole ship structural damage resulting from close-in underwater explosion shock, Mar. Struct. 31 (2013) 24–43, https://doi.org/10.1016/j.marstruc.2013.01.004.
[50] C.X. Qu, S.F. Ren, S.P. Wang, Q. Zhong, Numerical study on dynamic buckling of a cylindrical shell subjected to underwater explosion, Ocean Eng. 298 (2024), https://doi.org/10.1016/j.oceaneng.2024.116954.
[51] C. Yin, Z. Jin, Y. Chen, H. Hua, Shock mitigation effects of cellular cladding on submersible hull subjected to deep underwater explosion, Ocean Eng. 117 (2016) 221–237, https://doi.org/10.1016/j.oceaneng.2016.03.037.
[52] M.D.A. Hasan, Z.A.B. Ahmad, M.S. Leong, L.M. Hee, Enhanced frequency domain decomposition algorithm: a review of a recent development for unbiased damping ratio estimates, J. Vibroeng. 20 (2018) 1919–1936, https://doi.org/10.21595/jve.2018.19058.
[53] N.J. Jacobsen, P. Andersen, R. Brincker, Using enhanced frequency domain decomposition as a robust technique to harmonic excitation in operational modal analysis, in: Proceedings of ISMA2006: International Conference On Noise & Vibration Engineering, Katholieke Universiteit, 2006.
[54] W.M. Simpson, R.S. McCord, Teaching ship structures with maestro, in: Proceedings of the 2015 ASEE Annual Conference & Exposition, June 2015, pp. 26–1486.
[55] C.S. Smith, Influence of local compressive failure on ultimate longitudinal strength of a ship's hull, in: Proceedings of the International Symposium On Practical Design in Shipbuilding (PRADS), Tokyo, 1977, pp. 73–79, 17–21 October.
[56] O.A. Ullestad, Z. Liu, The application of the coupled acoustic–structural approach (CASA) method on the free vibration of submerged structures, Ocean Eng. 291 (2024), https://doi.org/10.1016/j.oceaneng.2023.116509.
[57] B. Nie, H. Zhang, Hoop and axial plastic buckling modes of submerged cylindrical shells subjected to side-on underwater explosion shock wave, Mar. Struct. 84 (2022), https://doi.org/10.1016/j.marstruc.2022.103200.
[58] G. Kyaw Oo D'Amore, M. Morgut, M. Biot, F. Mauro, J. Kašpar, Integration and optimization of the after-treatments systems to reduce the acoustic footprint of the ships, Appl. Acoust. 213 (2023), https://doi.org/10.1016/j.apacoust.2023.109625.
[59] L. Lin, X.D. Zhi, F. Fan, S.J. Meng, J.J Su, Determination of parameters of Johnson-cook models of Q235B steel, Zhendong Yu Chongji 33 (2014) 153–158, https://doi.org/10.13465/j.cnki.jvs.2014.09.028. +172.
[60] H. Wang, X. Zhu, Y.S. Cheng, J. Liu, Experimental and numerical investigation of ship structure subjected to close-in underwater shock wave and following gas bubble pulse, Mar. Struct. 39 (2014) 90–117, https://doi.org/10.1016/j.marstruc.2014.07.003.
[61] Vulkan Group, Official website, Available online: https://www.vulkan.com/it/, 2025. accessed on 26th January.
[62] T. Zhou, L. Cheng, A resonant beam damper tailored with acoustic black hole features for broadband vibration reduction, J. Sound Vib. 430 (2018) 174–184, https://doi.org/10.1016/j.jsv.2018.05.047.
[63] W. Jeon, S. Taehwan, P. Seongmin, Lightweight waveguide absorbers based on spiral acoustic black holes for reducing structural vibrations in mechanical systems. inter-noise and noise-con congress, Conf. Proc. 270 (2024) 10013–10016, https://doi.org/10.3397/IN_2024_4344.
[64] C. Zhao, M.G. Prasad, Acoustic black holes in structural design for vibration and noise control, Acoustics 1 (2019) 220–251, https://doi.org/10.3390/acoustics1010014.
[65] H. Ji, X. Zhao, N. Wang, W. Huang, J. Qiu, L. Cheng, A circular eccentric vibration absorber with circumferentially graded acoustic black hole features, J. Vib. Acoust. 144 (2) (2022) 021014, https://doi.org/10.1115/1.4053475.
[66] G. Rognoni, G.K.O. D'Amore, E. Brocco, L. Moro, M. Biot, Investigation on the impact of a metamaterial solution for the mitigation of noise radiated by a ship panel, in: ISOPE International Ocean and Polar Engineering Conference, ISOPE-I). ISOPE, 2023.
[67] X. Chen, J. Zhao, J. Deng, Y. Jing, H. Pu, J. Luo, Low-frequency enhancement of acoustic black holes via negative stiffness supporting, Int. J. Mech. Sci. (2023) 241, https://doi.org/10.1016/j.ijmecsci.2022.107921.